arXiv:1402.5571v1 [astro-ph.SR] 23 Feb 2014

The Astronomical Journal, in press

HUBBLE SPACE TELESCOPE INVESTIGATION OF MAIN-BELT COMET 133P/ELST-PIZARRO

David Jewitt[1,2], Masateru Ishiguro[3,1], Harold Weaver[4], Jessica Agarwal[5], Max Mutchler[6] and Steven Larson[7]

[1]*Dept. of Earth, Planetary and Space Sciences, University of California at Los Angeles, 595 Charles Young Drive East, Los Angeles, CA 90095-1567*

[2]*Dept. of Physics and Astronomy, University of California at Los Angeles, 430 Portola Plaza, Box 951547, Los Angeles, CA 90095-1547*

[3] *Dept. Physics and Astronomy, Seoul National University, Gwanak, Seoul 151-742, Republic of Korea*

[4] *The Johns Hopkins University Applied Physics Laboratory, 11100 Johns Hopkins Road, Laurel, Maryland 20723*

[5] *Max Planck Institute for Solar System Research, Max-Planck-Str. 2, 37191 Katlenburg-Lindau, Germany* [6] *Space Telescope Science Institute, 3700 San Martin Drive, Baltimore, MD 21218*

[7] *Lunar and Planetary Laboratory, University of Arizona, 1629 E. University Blvd. Tucson AZ 85721-0092*

jewitt@ucla.edu

ABSTRACT

We report new observations of the prototype main-belt comet (active asteroid) 133P/Elst-Pizarro taken at high angular resolution using the Hubble Space Telescope. The object has three main components; a) a point-like nucleus, b) a long, narrow antisolar dust tail and c) a short, sunward anti-tail. There is no resolved coma. The nucleus has a mean absolute magnitude $H_V = 15.70 \pm 0.10$ and a lightcurve range $\Delta V = 0.42$ mag., the latter corresponding to projected dimensions 3.6×5.4 km (axis ratio 1.5:1), at the previously measured geometric albedo of 0.05±0.02. We explored a range of continuous and impulsive emission models to simultaneously fit the measured surface brightness profile, width and position angle of the antisolar tail. Preferred fits invoke protracted emission, over a period of 150 days or less, of dust grains following a differential power-law size distribution with index $3.25 \leq q \leq 3.5$ and having a wide range of sizes.

Ultra-low surface brightness dust projected in the sunward direction is a remnant from emission activity occurring in previous orbits, and consists of the largest ($\geq$cm-sized) particles. Ejection velocities of one micron-sized particles are comparable to the ~ 1.8 m s^{-1} gravitational escape speed of the nucleus, while larger particles are released at speeds less than the gravitational escape velocity. The observations are consistent with, but do not prove, a hybrid hypothesis in which mass loss is driven by gas drag from the sublimation of near-surface water ice, but escape is aided by centripetal acceleration from the rotation of the elongated nucleus. No plausible alternative hypothesis has been identified.

Subject headings: minor planets, asteroids: general — minor planets, asteroids: individual (133P/Elst-Pizarro) — comets: general — meteorites, meteors, meteoroids

1. INTRODUCTION

In the traditional view, asteroids are rocky bodies formed inside the snow line of the Sun's proto-planetary disk while comets are ice-containing objects formed outside it. Recently, several hybrid objects having orbits interior to Jupiter's and the dynamical properties of asteroids, have been found to exhibit comet-like mass-loss (Hsieh and Jewitt 2006). Known as main belt comets (MBC) or, more generally, active asteroids (Jewitt 2012), these objects are candidate ice-bearing asteroids. Asteroid ice is of potentially far-reaching scientific interest. Most importantly, the outer regions of the asteroid belt may have supplied some Terrestrial water and other volatiles, including the biogenic precursor molecules up to and including amino acids (Mottl et al. 2007). In the modern solar system, there is no known dynamical path linking stable orbits in the asteroid belt to the classical comet reservoirs in the Kuiper belt or Oort cloud. Instead, if ice exists in the asteroid main belt, it is likely to be primordial, trapped either at the formation epoch, or in some early, chaotic phase of solar system history (Levison et al. 2009).

About a dozen examples of active asteroids are currently known, but they do not all contain ice. Data in-hand already clearly show the action of several different processes in causing mass-loss, ranging from asteroid-asteroid impact, to rotational break-up, to thermal fracture and more (Jewitt 2012). Only for two objects, 133P/Elst-Pizarro (Hsieh et al. 2004, Hsieh and Jewitt 2006, Hsieh et al. 2010) and 238P/Read (Hsieh and Jewitt 2006, Hsieh et al. 2011), is the evidence for water sublimation reasonably strong. The most compelling evidence is the repeated activity exhibited by both bodies. This is naturally explained by the seasonal sublimation of near-surface ice (including effects due to the orbital eccentricity as

well as the obliquity of the nucleus, and possible self-shadowing by surface topography) but is difficult or impossible to reconcile with the other mass-loss mechanisms so far envisioned. No gas has yet been spectroscopically detected in any of the active asteroids, but the available limits to gas production are consistent with the very low ($<$1 kg s^{-1}) mass-loss rates inferred from dust (Jewitt 2012). The evidence for ice sublimation thus remains indirect but no other plausible explanation for the observations, in particular for the seasonal recurrence of the activity, is known.

In this paper we describe the first high angular resolution, time-resolved images of 133P obtained using the Hubble Space Telescope. Our observations were triggered by the report of new activity on UT 2013 June 4, the fourth such episode of activity in 133P observed since 1996 (Hsieh et al. 2013). We use the images to examine in detail the spatial and temporal properties of the mass-loss in the near-nucleus environment and to test the viability of the sublimating ice hypothesis.

2. OBSERVATIONS

We used two consecutive orbits of Target-of-Opportunity time (General Observer program number 13005) to observe 133P on UT 2013 July 10. Consecutive orbits were secured in a deliberate attempt to observe time-dependent changes in the inner coma, as might be induced by the rotation of the underlying nucleus at period 3.471$\pm$0.001 hr (Hsieh et al. 2004). We obtained a total of 12 images with the WFC3 camera (Dressel 2010). The 0.04″ pixels of WFC3 each correspond to about 60.2 km at the distance of 133P, giving a Nyquist-sampled spatial resolution of about 120 km. All observations were taken using the F350LP filter. This very broad filter (full-width-at-half-maximum is 4758Å, while the effective wavelength for a solar-type (G2V) source is 6230Å) provides maximum sensitivity to faint sources at the expense of introducing some uncertainty in the transformation to standard astronomical filter sets. We used the HST exposure time calculator to convert the measured count rate into an effective V magnitude, finding that a V = 0 G2V source gives a count rate of 4.72 $\times 10^{10}$ s^{-1} within a 0.2″ radius photometry aperture.

The observational geometry of the HST observations is summarized in Table (1).

3. DERIVED PROPERTIES OF 133P

Figure (1) shows the drizzle-combination of all 12 exposures. Cosmic rays and most background objects have been successfully removed from Figure (1) except for residual signals

from spatially extended objects (galaxies), some of which cross the tail obliquely ($G1$ and $G2$ in the Figure). 133P shows its characteristic point-like nucleus, while a thin, straight dust tail extends >60″ (90,000 km) to the edge of the field of view along position angle 247.1°±0.4°. The position angles of the projected antisolar direction and the negative velocity vector were 246.8° and 248.7°, respectively. These directions are so close as to be indistinguishable in Figure 1.

3.1. Nucleus

The light from the central region is dominated by the bright and point-like nucleus. Figure (2) shows aperture photometry measured from the individual images, after cleaning by hand for the removal of cosmic rays and artifacts. To perform the latter, we first subtracted the median image from each individual image, in order to make visible cosmic rays and artifacts otherwise hidden in the bright near-nucleus region. Then we removed cosmic rays one by one, using digital interpolation to replace affected pixels with the means of their surroundings. Lastly, we added back the median image in order to recover the total signal. For photometry, we used apertures 5 pixels (0.2″) and 25 pixels (1.0″) in radius, with sky subtraction determined from the median signal computed within a concentric annulus having inner and outer radii 25 and 50 pixels (2.0″), respectively. We refer to magnitudes from these apertures as $V_{0.2}$ and $V_{1.0}$, respectively. The use of such small apertures is enabled by the extraordinary image quality and pointing stability of the Hubble Space Telescope. Photometry with the 0.2″ aperture samples primarily the nucleus, with only a small contribution from the surrounding dust. Photometry with the 1.0″ aperture includes both nucleus and dust, and is useful to compare with ground-based data in which atmospheric seeing precludes the use of sub-arcsecond apertures. Figure (2) shows a clear temporal variation in both $V_{0.2}$ and $V_{1.0}$.

The photometry and the physical properties of the comet are connected by the inverse square law of brightness, written

$$p_V \Phi(\alpha) C_n = 2.25 \times 10^{22} \pi R^2 \Delta^2 10^{-0.4(m-m_\odot)} \quad (1)$$

where R, Δ and α are from Table (1), $\Phi(\alpha)$ is the phase function correction and $m_\odot$ = -26.75 is the apparent V magnitude of the Sun (Drilling and Landolt 2000). The physical properties are the V-band geometric albedo, p_V, and the effective cross-section of the nucleus, C_n. The albedo of 133P is $p_V = 0.05 \pm 0.02$ (Hsieh et al. 2009). For the correction to 0° phase angle we use the measured (H,G) phase function from Figure 3 of Hsieh et al. (2010), which gives

1.1±0.1 mag., corresponding to $\Phi(18.7^\circ) = 0.36\pm0.03$.

The 0.2″ aperture gives our best estimate of the nucleus brightness, with only minimal contamination from the near-nucleus dust. We estimate that the mean apparent magnitude is V = 20.55±0.05 (Table 2). The resulting absolute magnitude (at R = Δ = 1 AU and $\alpha = 0^\circ$) is $H_V = 15.70\pm0.10$. Substituting into Equation (1) we obtain the nucleus cross-section $C_n = 15\pm5$ km^2 and the equivalent circular radius $r_n = (C_n/\pi)^{1/2} = 2.2\pm0.5$ km. The uncertainties on both numbers are dominated by uncertainty in p_V, itself a product of phase-function uncertainty. The full range of the measured lightcurve in Figure (2) is $\Delta V = 0.42$ mag. If attributed to the rotational variation of the cross-section of an $a \times b$ ellipsoid, then $a/b = 10^{0.4\Delta V} = 1.5$, with $a \times b = 2.7 \times 1.8$ km. Formally, the axis ratio derived from the lightcurve is a lower limit to the true value because the HST sampling missed minimum light and because we observe only the projection of the true nucleus axis ratio into the plane of the sky. In practice, no larger ΔV has been reported for 133P (Hsieh et al. 2004, 2009, 2010, Bagnulo et al. 2010); we suspect that 133P is viewed from a near-equatorial perspective and that $a/b = 1.5$ is close to the true nucleus axis ratio.

The minimum density needed to ensure that the material at the tips of a prolate body in rotation about its minor axis is gravitationally bound is approximately

$$\rho_n \sim 1000 \left(\frac{3.3}{P}\right)^2 \left[\frac{a}{b}\right] \tag{2}$$

where P is the rotation period in hours (Harris 1996). Substituting $P = 3.5$, $(a/b) = 1.5$, we find $\rho_n \sim 1300$ kg m^{-3}, identical to a value determined from ground-based data (Hsieh et al. 2004). The relation between the derived density and the true bulk density of 133P is uncertain, pending determination of the strength properties of the nucleus.

3.2. Dust Tail and Near-Nucleus Environment

We also plot in Figure (2) the effective magnitude of the material projected between the 0.2″ and 1.0″ annuli, computed from

$$V(0.2, 1.0) = -2.5 \times \log_{10}\left[10^{-0.4V_{0.2}} - 10^{-0.4V_{1.0}}\right]. \tag{3}$$

Evidently, the coma in the 0.2″ to 1.0″ annulus is steady or slightly increasing in brightness with time and does not share the temporal variability exhibited by the nucleus itself. This is most likely because spatial averaging inhibits our ability to detect rotational modulation

in the dust ejection rate. To see this, assume that the dust ejection speeds are comparable to the nucleus gravitational escape speed, $V_e \sim 1$ m s^{-1}. The time taken for dust to cross the photometry annulus is $\tau_c \sim \delta r / V_e$, where $\delta r \sim 10^3$ km is the linear distance between the $0.2''$ and $1.0''$ radius apertures. We find $\tau_c \sim 10^6$ s, far longer than the $P \sim 10^4$ s nucleus rotation period. Therefore, the photometry annulus should contain dust produced over $\tau_c / P \sim 10^2$ nucleus rotations, effectively smoothing out any rotation-dependent modulation of the signal.

Figure (1) hints at the presence of several near-nucleus dust structures. To examine these, we need to consider diffraction in the telescope optics and other artifacts. For this purpose, we computed point-spread function (PSF) models using the "TinyTim" software package (Krist et al. 2011). We assumed a G2V stellar spectrum and centered and scaled the model PSF to the data using photometry extracted from a circular aperture of projected radius 2 pixels. The optimum scaling and centering were rendered slightly uncertain by the near-nucleus morphology of 133P. We experimented with different scale factors and centers, finding that the results presented here are stable with respect to these factors. The resulting difference image (Figure 3b) successfully removes the diffraction spikes B and E. Feature D is an artifact caused by imperfect charge-transfer efficiency in the WFC3 detector and not modeled in the TinyTim software (c.f. Weaver et al. 2010). Another diffraction spike underlies feature C, but residual emission survives in the difference image. A lightly-smoothed version of Figure 3b is shown in Figure 3c, to emphasize the faint, surviving feature C. We conclude that the major, measurable components of the image of 133P are 1) the nucleus, 2) the main tail, A, to the west of the nucleus and 3) a stubby, sunward tail, C, to the east. The nucleus and the main tail have been defining signatures of 133P in all previous observations of 133P when in its active state (Hsieh et al. 2004). The sunward tail has not been previously reported.

No coma is visually apparent in the HST data. The 1.6 pixel ($0.064''$) full-width-at-half maximum of the TinyTim model PSF is very close to the 2.2 pixels ($0.086''$) FWHM of the combined 133P image, measured in the same way. The absence of a coma is a clear indicator of the extremely low velocities with which dust particles are ejected from 133P. A crude estimate of these velocities is obtained by considering the turn-around distance of a particle ejected towards the Sun at speed v, which is given by $X_R = v^2/(2\beta g_\odot)$ (Jewitt and Meech 1987). Dimensionless factor β is a function of particle size, approximately given by $\beta \sim 1/a_{\mu m}$, where $a_{\mu m}$ is the grain radius expressed in microns. Substitution gives

$$v^2 a_{\mu m} = 2 g_\odot X_R \tag{4}$$

as a constraint on the particles that can be ejected from the nucleus of 133P. Substituting

$X_R < 150$ km (0.1″) and $g_\odot = 8{\times}10^{-4}$ m s^{-2} for $R = 2.7$ AU, we obtain $v^2 a_{\mu m} < 240$ m^2 s^{-2}. For instance, with $a_{\mu m} = 1$, we find $v < 15$ m s^{-1} while millimeter-sized particles, $a_{\mu m} = 1000$, have $v < 0.5$ m s^{-1}. The absence of a resolved coma therefore requires that particle ejection speeds be far smaller than the expected thermal speed of gas molecules ($V_g \sim 500$ m s^{-1}) at this heliocentric distance. We will reach a similar conclusion, later, in consideration of the narrow width of the tail of 133P. For comparison, a short-period comet at similar distance might have $X_R \sim 3{\times}10^7$ m (Jewitt and Meech 1987), giving $v^2 a_{\mu m} \sim 5{\times}10^4$ m^2 s^{-2}. For a given particle size, $a_{\mu m}$, the dust from 133P is ejected sunward about $(5{\times}10^4/240)^{1/2} \sim 15$ times or more slowly than from the short period comet. Non-detection of a coma is our first indication of the very low dust speeds in 133P.

We further examined the near-nucleus region in search of dust structures that might be carried around by the rotation of the nucleus. For this purpose, we subtracted the median image from the individual images in order to enhance temporal and spatial changes. We found by experiment that centering uncertainties as small as ±0.1 pixel (0.004″) had a large influence in the resulting difference images, to the extent that we could not reliably identify any evidence for a rotating pattern of emission.

4. DUST MODELS

4.1. Order of Magnitude Considerations

The observed length of the main tail is $\ell_T \gtrsim 90{,}000$ km. This is a lower limit to the true length both because the tail extends beyond the field of view of HST and because we observe only the projection of the tail in the plane of the sky. The time taken for radiation pressure to accelerate a grain over distance ℓ_T is $\tau_{rp} \sim (2\ell_T/\alpha_g)^{1/2}$, where α_g is the grain acceleration. We write $\alpha_g = \beta g_\odot$, where $g_\odot = 8 \times 10^{-4}$ m s^{-2} is the gravitational acceleration to the Sun at the heliocentric distance of 133P. Substituting $\beta \sim 1/a_{\mu m}$, we find that the radiation pressure timescale for the main tail is $\tau_{rp} \sim 5 \times 10^5 a_{\mu m}^{1/2}$ s. A 1 μm grain would be swept from the tail in $5{\times}10^5$ s (∼6 days) while a 100 μm grain would take ∼2 months to be removed. Equivalently, if we suppose that the main tail consists of particles ejected no earlier than the date on which the present active phase of 133P was discovered, UT 2013 June 4 (Hsieh et al. 2013), then the particle size implied by the length of the tail is $a_{\mu m} \sim 50$ μm. This is a lower limit to the particle size because larger particles (smaller β) would not have reached the end of the tail, and because the tail is certainly older than the June 4 date of discovery. While clearly very crude, this estimate shows that the particles in the tail are larger than those typically observed at optical wavelengths and provides a basis for comparison with more sophisticated calculations, described in Section 4.2.

The width of the antisolar tail was measured from a series of profiles extracted perpendicular to the tail. We binned the data parallel to the tail in order to increase the signal-to-noise ratio of the measurement, with larger bin sizes at the distant, fainter end of the tail than near the nucleus. The width was estimated from the FWHM of the profiles and is shown in Figure (5). The Figure shows estimated statistical uncertainties on the widths, but these underestimate the total uncertainties, which include significant systematic effects due to background sources. The trail width increases from $\theta_w = 0.2''$ (width $w_T \sim 300$ km) near the nucleus to $\theta_w = 0.5''$ ($w_T \sim 800$ km) $13''$ west along the tail. The very faint sunward tail was also measured, albeit with great difficulty (Figure 5).

At the time of observation, Earth was only 0.54° below the orbital plane of 133P (Table 1), so that w_T largely reflects the true width of the tail perpendicular to the orbit. The width of the dust tail is related to V, the component of the dust ejection velocity measured perpendicular to the orbital plane, by $w_T = 2\ V\delta t$, where δt is the time elapsed since release from the nucleus, provided $\delta t \ll$ the orbital period of 133P. The factor of 2 arises because particles are ejected both above and below the orbital plane. We write $V = V_1/a_{\mu m}^{1/2}$, where V_1 is the perpendicular ejection velocity of an $a_{\mu m} = 1$ particle. Assuming that the dust motion parallel to the orbit plane is determined by radiation pressure acceleration, we may write the distance of travel from the nucleus as $\ell_T = (1/2)\beta g_\odot \delta t^2$. Again, setting $\beta \sim 1/a_{\mu m}$, we can eliminate δt between these equations to find

$$V_1 = \left(\frac{g_\odot w_T^2}{8\ell_T} \right)^{1/2} \tag{5}$$

Equation (5) shows that $w_T \propto \ell_T^{1/2}$, broadly consistent with the trend of the measurements in Figure (5). We fitted Equation (5) to the width vs. length data plotted in Figure (5), finding $V_1 = 1.8$ m s^{-1} and hence

$$V(a) = \frac{1.8}{a_{\mu m}^{1/2}}\ [m\ s^{-1}] \tag{6}$$

This estimate is made assuming that the tail lies in the plane of the sky, and hence that the measured length is not foreshortened. Equation (6) gives extraordinarily small velocities compared to the sound speed in gas ($V_g \sim 500$ m s^{-1}), and implies $V(1\ mm) \sim 6$ cm s^{-1} for 1 mm particles and $V(1\ cm) \sim 1.8$ cm s^{-1} for centimeter-sized grains. We will return to this point in Section 5.

We extracted the surface brightness along the tail within a 41 pixel ($1.64''$) wide rectangular box aligned parallel to the tail axis. Sky subtraction was obtained from a linear

interpolation of the background in equal-sized regions above and below the tail. The surface brightness profile, shown in Figure (4), is normalized to a peak value $\Sigma_0 = 15.80$ V mag. (arcsec)$^{-2}$. The surface brightness as a function of distance, d, along the tail is consistent with $\Sigma \propto d^{\gamma}$, where γ=-0.86±0.06 and $30 \leq d \leq 200$ pixel ($1.2 \leq d \leq 8.0''$). The measurements become unreliable beyond about 16″ west of the nucleus, owing to a combination of extreme faintness and overlap by the images of imperfectly-removed field galaxies (c.f. Figure 1). The surface brightness drops precipitously to the east of the nucleus but, as noted above, dust is evident within a few arcseconds as Feature "C" (Figure 1).

We measured the ratio of the light scattered from the dust to that scattered from the nucleus. Given that the nucleus and dust have the same albedo and phase function, this brightness ratio is equivalent to the ratio of the dust cross-section to the nucleus cross-section, C_d/C_n. We find $C_d/C_n = 0.36$, with an uncertainty that is dominated by systematics of the data and is difficult to estimate, but is unlikely to be larger than 50%. With nucleus cross-section $C_n = 15\pm2$ km^2, we find $C_d = 5.4$ km^2, good to within a factor of two. We will use this cross-section to estimate the dust mass in Section 5.

4.2. Dynamical Tail Models

To advance beyond the order of magnitude considerations in Section 4.1, we created model images of 133P using a Monte Carlo dynamical procedure developed in Ishiguro et al. (2007) and Ishiguro et al. (2013). It is not possible to obtain unique solutions for the dust properties from the models, given the large number of poorly constrained parameters in the problem. However, the numerical models are useful because they can help reveal implausible solutions, and identify broad ranges of dust ejection parameters that are compatible with the data.

The dynamics of dust grains are determined both by their ejection velocity and by the radiation pressure acceleration and solar gravity, parametrized through their ratio, β. For spherical particles, $\beta = 0.57/\rho a_{\mu m}$, where ρ is the dust mass density in g cm^{-3} (Burns et al. 1979). In the rest of the paper, we assume the nominal density $\rho = 1$ g cm^{-3} and compute particle radii in microns, $a_{\mu m}$, accordingly. We assume that dust particles are ejected symmetrically with respect to the Sun–comet axis in a cone-shape distribution with half-opening angle ω and that the ejection speed is a function of the particle size and, hence, of β. We adopt the following function for the terminal speed:

$$V_T = vV_1\ \beta^{u_1}, \tag{7}$$

where V_1 is the average ejection velocity of particles having β=1. As considered in Ishiguro et al. (2007), V_T also has a heliocentric distance dependence. Here, we neglect this dependence because the eccentricity of 133P, e=0.16, is small and the R dependence of V_T is weak. The power index, u_1, characterizes the β (i.e. size) dependence of the ejection velocity. In Equation (7), v is a random variable in which the probability of finding v in the range v to $v + dv$ is given by the Gaussian density function, $P(v)dv$,

$$P(v)dv = \frac{1}{\sqrt{2\pi}\sigma_v} \exp\left[-\frac{(v-1)^2}{2\sigma_v^2}\right] dv, \tag{8}$$

where σ_v is the standard deviation of v. Two thirds of the values fall within $\pm 1\sigma_v$ of the mean. A power-law size distribution with an index q was used. The dust production rate at given size and time is written:

$$N(a_{\mu m}; t)\ da = N_0\ a_{\mu m}^{-q} R^{-k}\ da, \tag{9}$$

in the size range of $a_{min} \leq a_{\mu m} \leq a_{max}$, where $a_{min} = 0.57/\rho\beta_{max}$ and $a_{max} = 0.57/\rho\beta_{min}$, respectively. The power index, k, defines the dust production rate as a function of the heliocentric distance R, and R is calculated as a function of time t. In Equation (9), R is expressed in AU.

Model images were produced by Monte Carlo simulation by solving Kepler's equation including solar gravity and radiation pressure. We calculated the positions of dust particles on UT 2013 July 10 under conditions given by Equation (7)–(9), and derived the cross-sectional areas of dust particles in the HST/WFC3 CCD coordinate system by integrating with respect to time and particle size, that is,

$$C(x, y) = \int_{t_0}^{t_1} \int_{a_{min}}^{a_{max}} N_{cal}(a_{\mu m}, t, x, y)\ \pi a_{\mu m}^2\ da_{\mu m}\ dt \tag{10}$$

where $N_{cal}(a_{\mu m}, t, x, y)$ is the number of dust particles projected within a pixel at coordinates (x,y) in a WFC3 CCD image. The model assumes that dust is ejected uniformly over the interval from t_0 to t_1, such that t_0 is the time elapsed between the start of dust ejection and our HST observation, and t_1 is the time elapsed between the end of dust ejection and our HST observation.

The HST data offer four key properties with which to constrain our dust models:

1. The position angle of the tail is $\theta_{PA} = 247.1° \pm 0.4°$ on UT 2013 July 10.

2. No gap can be discerned between the nucleus and the dust tail. Any such gap larger than $\sim$0.4″ would be easily detected.

3. The surface brightness profile of the tail can be approximately represented by $\Sigma \propto d^{\gamma}$, where γ = -0.86±0.06 and 30 $\leq d \leq$200 pixel (1.2 $\leq d \leq$ 8.0″; c.f. Figure 4).

4. The full width at half maximum of the antisolar tail is very small, rising from 0.2″ near the nucleus to 0.5″ 12″ to the west (c.f. Figure 5).

As a starting point, we used the model parameters derived by Hsieh et al. (2004). They assumed u_1=1/2, appropriate for gas-driven dust ejection and a power-law differential size distribution with an index of q =3.5 in the range $0.05 < \beta < 0.5$. Hsieh et al. (2004) noticed that the tail width was controlled by the particle ejection velocity perpendicular to the orbital plane, V_1, finding $V_1 = 1.1$ m s^{-1}. We examined the width and surface brightness to compare with our observational results assuming $\omega = 90^{\circ}$ and $V_1 = 1.5$ m s^{-1}. We arbitrarily chose t_0 = 1177 days (time of the last aphelion passage) and t_1=0. Figure (5) shows that the Hsieh et al. (2004) model parameters approximately match the dust trail width in the HST data. However, Figure 6 shows that the model fails to match the new surface brightness profile.

To try to improve the fit, we examined which parameters in our model most affect the observed quantities. In our model the tail width is largely controlled by $V_1 \sin w$. The position angle of the dust tail is largely a measure of the timing and duration of dust ejection (t_0 and t_1). The surface brightness distribution depends on the starting time and duration of dust ejection (t_0 and t_1), the size range of the particles (β_{min} and β_{max}) and the size distribution index (q). When dust particles are ejected at constant rate over a long interval (specifically, for a time longer than the time needed for the slowest dust particles to travel the length of the tail), a steady-state flow of dust particles results in a surface brightness distribution with γ = -0.5 (Jewitt and Meech 1987). On the other hand, short-term dust supply creates a steeper surface brightness distribution, i.e. $\gamma < -0.5$, because larger, slower particles are bunched-up near the nucleus increasing the surface brightness there.

A key question is whether dust emission from 133P was impulsive (as would be expected from an impact, for example) or continuous (more consistent with sublimation-driven mass-loss). We computed two families of models to attempt to address this question. In the continuous ejection models (CM), the dust ejection is supposed to be steady in the interval from the start time, t_0, to the end time, t_1, and we assume $t_1 = 0$, corresponding to dust emission continuing up to the epoch of observation. In the impulsive ejection models (IM), we limit the dust ejection to a single day (i.e. dust is released from t_0 to t_1=t_0-1) to approximate an impulse. We created simulation images using a wide range of parameters as listed in Table (3).

As mentioned above, the tail position angle, θ_{PA}, is largely determined by the ejection epoch. Figure (7) shows θ_{PA} as a function of t_0 for the CM and IM models. Also shown in the figure is the observed range of tail position angles, measured from the HST data. We find that, to be consistent with the measured θ_{PA}, continuous ejection must have started within 150 days of the HST observation on July 10 (i.e. $t_0 \leq 150$ days). In the case of impulsive ejection, dust release must have occurred within 70 days of the HST observation ($t_0 \leq 70$ days) in order to fit the measured tail position angle. Separately, the detection of dust on June 4 by Hsieh et al. (2013), 36 days prior to our Hubble observation, indicates $t_0 > 36$ days (this is probably a very strong limit to t_0 since Hsieh already reported a 50″ tail on June 4). We therefore conservatively conclude that $36 \leq t_0 \leq 150$ days and $36 \leq t_0 \leq 70$ days, for the continuous and impulsive dust models, respectively. The age of the dust is measured in months, not years or days. Unfortunately, the tail position angle alone does not provide convincing discrimination between the continuous and impulsive ejection models.

More stringent constraints can be set from the dust trail surface brightness profile, from the absence of a near-nucleus coma-gap and from the measured tail width. In CM, we found no model parameter sets that satisfy the observational constraints (1) to (4) when $q \geq 3.5$ while only 2% satisfy the constraints when $q = 3.0$ is assumed. However, 28% of the tested parameter sets satisfied these conditions when $q = 3.25$; we believe that $3.25 \leq q \leq 3.5$ best represents the size distribution index for the continuous emission models. For continuous ejection models having $t_0 = 36$ days, we find $2{\times}10^{-3} \leq \beta \leq 7{\times}10^{-2}$, corresponding to particle radii $10 \leq a \leq 300$ μm. For continuous ejection beginning at $t_0 = 150$ days, we find $6{\times}10^{-5} \leq \beta \leq 3{\times}10^{-3}$, corresponding to particle radii $0.2 \leq a \leq 10$ mm.

The observed tail surface brightness gradient, γ, correlates strongly with q, as shown in Figure (8). The filled circles denote the average values from our model results with their 3 σ uncertainties. The point at $q = 3.15$ (open circle in Figure (8)) matches the measured surface brightness index, γ=-0.86±0.06. Impulsive models with $q = 3.15{\pm}0.05$ can match the surface brightness gradient of the tail. However, large (slow) particles are needed to avoid the growth of a gap between tail and nucleus, as shown in Figure 9. Assuming that any such gap is smaller than 10 pixel (0.4″), we estimate $\beta_{min} \leq 4{\times}10^{-4}$ (t_0=36) to $1{\times}10^{-4}$ (t_0=70), which correspond to $a_{max} \geq 1.4$ mm – 5.7 mm. Such particles are a factor of ten or more larger than those inferred in earlier work. These models successfully match the observed brightness distribution and the measured tail width. Figure (5) compares the observed and model tail widths.

While the multi-parameter nature of the dust modeling allows us to find impulsive ejection models to fit the imaging data, the photometry imposes an important, additional constraint. In the impulsive case, the scattering cross section near the nucleus should decrease

with time as a result of radiation pressure sweeping and the absence of a source of dust particle replenishment. Instead, the coma magnitude in the 0.2″–1.0″ annulus shows no evidence for fading with time (Figure 2). Furthermore, the HST photometry (Table 2) is consistent with the brightness determined in the June 04 - 14 period by Hsieh et al. (2013), which itself showed no evidence for fading. The absence of fading is hard to understand in the context of an impulsive ejection origin, except by highly contrived means (e.g. ejected particles could brighten by fragmenting in such a way as to offset the fading caused by radiation pressure sweeping). We conclude that it is very unlikely that the dust ejection was impulsive. Protracted emission was independently inferred from observations of 133P in previous orbits (Hsieh et al. 2004, 2010) and is consistent with dust ejection through the production of sublimated ice.

The sunward tail (Feature "C" in Figure 3) is not present in our basic simulations of 133P because all particles are quickly accelerated to the antisunward side of the nucleus by radiation pressure. We considered two possibilities to explain the existence of the sunward tail. First, high speed dust particles could be launched sunward in a narrow jet (to maintain $V_1 \sin w$, needed to ensure a narrow tail and no resolvable coma). By experiment we find that a half-opening angle $\omega \ll 5^\circ$ would be needed to produce Feature "C" in Figure 3, but, while this solution is technically possible, it seems contrived. We favor a second possibility, namely that the sunward tail consists of ultra-large, slow particles ejected during a previous orbit. Particles released from the nucleus and moving largely under the action of solar gravity will return to the vicinity of the orbit plane every half orbit period, producing a structure known as a "neck-line" (Kimura and Liu 1977). Our second possibility is that Feature "C" could be 133P's neck-line, produced by the convergence of particles released a full orbit ago. If so, we estimate that the responsible particles in region C have sizes measured in centimeters or larger. A simulation of the neck-line structure is shown in Figure (11).

5. DISCUSSION

5.1. Particle Properties: Mass, Loss Rate and Lifetime

We estimate the dust mass in 133P as follows. The mass of an optically thin collection of spheres of individual density ρ and mean radius $\overline{a}$ is related to their total cross-section, C_d, by $M_d = 4/3\rho\overline{a}C_d$. The effective mean radius of the particles contributing to the scattered light depends on the size distribution, $N(a)da$, the scattering area, πa^2, and the time of residence of particles in the tail. The latter is size-dependent because radiation pressure imparts a velocity to dust particles that scales as $V = V_1/a^{1/2}$, where V_1 is a constant. The amount of time that a particle of size a spends in a given pixel of size δx is $t = \delta x/V =$

($Ka^{1/2}$), where K is a constant. Putting these together, we find that the effective mean particle radius weighted by the size distribution, the scattering cross-section and the time of residence is

$$\overline{a} = \frac{\int_{a_{min}}^{a_{max}} a\pi a^2 K a^{1/2} N(a) da}{\int_{a_{min}}^{a_{max}} \pi a^2 K a^{1/2} N(a) da} \tag{11}$$

with $N(a)$ computed from Equation 9. The continuous ejection models give $3.25 \leq q \leq 3.5$ (Table 3). With these values, and assuming $a_{max} \gg a_{min}$, we obtain

$$\overline{a} \sim \frac{a_{max}}{5};\ (q = 3.25) \tag{12}$$

$$\overline{a} \sim \frac{a_{max}}{\ln(a_{max}/a_{min})};\ (q = 3.5) \tag{13}$$

For example, in continuous emission starting at $t_0 = 150$ days, with $0.2 \leq a \leq 10$ mm (Table 3), Equations (12) and (13) give $\overline{a} = 2$ to 3 mm. With $\rho = 1000$ kg m^{-3}, we estimate the mass in the particle tail as $M_d \sim 1.8\times10^7$ kg. If this mass were released uniformly over $\sim$150 days, the implied mean mass-loss rate would be $dM_d/dt \sim 1.4$ kg s^{-1}, consistent with previous estimates of the mass-loss rates in 133P. The corresponding values for the $t_0 = 36$ day solution are $\overline{a} = 60$ to 90 μm, $M_d \sim 5\times10^5$ kg and $dM_d/dt \sim 0.2$ kg s^{-1}. We conclude that the continuous emission models bracket the mass-loss rates in the range $0.2 \leq dM_d/dt \leq 1.4$ kg s^{-1}. These rates are 10 to 100 times larger than found by Hsieh et al. (2004), largely because they used much smaller mean dust grain sizes than found here.

The mass-loss lifetime of the nucleus 133P can be estimated from

$$\tau = \frac{M_n}{f_o f_a (dM_d/dt)} \tag{14}$$

in which M_n is the mass of the nucleus, f_o is the fraction of each orbit over which 133P ejects mass and f_a is the duty cycle (ratio of active periods to elapsed time) for mass-loss between orbits. The mass of a 2 km radius spherical nucleus of density $\rho = 1300$ kg m^{-3} is $M_n \sim 4\times10^{13}$ kg. Observations show that $f_o \sim 0.2$ (Toth 2006) while f_a is unknown. Substituting into Equation (14), and expressing τ in years, we find $5\times10^6 \leq \tau f_a \leq 3\times10^7$ yr. Strong upper limits to the duty cycle are obtained by setting $\tau = 4.5\times10^9$ yr, the age of the solar system. Then, we must have $f_a < 0.001$ for ice in 133P to survive for the age of the solar system. This limit is consistent with most current (albeit widely scattered) observational

limits from ensemble asteroid observations, according to which the instantaneous ratio of active to inactive asteroids is 1:6 to 1:60 (Hsieh 2009), <1:300 (Hsieh and Jewitt 2006), <1:400 (Sonnet et al. 2011), <1:25,000 (Gilbert and Wiegert 2010) and <1:30,000 (Waszczak et al. 2013). It has been suggested that 133P might be a product of a recent ($\lesssim$10 Myr) asteroid-asteroid collision (Nesvorny et al. 2009). If so, the preservation of ice would be trivial even for much larger duty cycles.

5.2. Ejection Mechanism

The main observation suggesting that sublimation drives mass loss from 133P is the seasonal recurrence of activity. Episodes of mass loss have repeated in the months near and immediately following perihelion in four consecutive orbits but mass loss was absent in between (Hsieh et al. 2004, Hsieh and Jewitt 2006, Hsieh et al. 2010, Hsieh et al. 2013). Recurrence at a particular orbital phase strongly suggests a thermal trigger for the activity, and is reminiscent of the orbitally modulated mass loss observed in "normal" comets from the Kuiper belt. None of the other mechanisms considered as drivers of mass loss from the active asteroids (including impact, rotational breakup, electrostatic ejection, thermal fracture and desiccation cracking) can produce seasonal activity on 133P in any but the most contrived way (Jewitt 2012). Separately, the protracted nature of the emission in 133P is not readily explained by the other mechanisms but it is natural for sublimating ice. Furthermore, we obtained good model fits to the data when assuming a drag-like size-velocity relation ($V \propto a^{-1/2}$) but not when using a V = constant velocity law. The multi-parameter nature of the dust modeling problem means that we cannot formally exclude other size-velocity laws, but the success of the drag-like relation is at least consistent with a gas drag origin. Lastly, Chesley et al. (2010) reported a 3σ confidence detection of non-gravitational acceleration in 133P, most simply interpreted as a rocket effect from asymmetric sublimation.

However, the immediate problem for gas drag is that the solid particles are launched much more slowly than expected. Micron-sized grains reach only $V_1 \sim 1$ m s^{-1}, as shown both by the order of magnitude approach in Section (4.1) and by the detailed models in Section (4.2) (see also Figure 5). This is quite different from active comets near the sun, in which micron-sized particles are dynamically well-coupled to the outflowing gas and attain terminal velocities comparable to the local gas velocity while even centimeter-sized grains exceed 1 m s^{-1} (Harmon et al. 2004). Whipple's (1951) model has become the first stop for estimating comet dust velocities (e.g. Agarwal et al. 2007). Applied to 133P, his model predicts the speed of micron-sized particles as $V_1 \gtrsim 100$ m s^{-1} while millimeter grains should travel at 4.5 m s^{-1}, about two orders of magnitude faster than measured.

To examine the problem of the ejection speed more closely, we consider sublimation from an exposed patch of ice located at the subsolar point on 133P. We solved the energy balance equation for a perfectly absorbing ice surface exposed at the subsolar point, with 133P located at 2.725 AU. We included heating and cooling of the surface by radiation and cooling by latent heat taken up as the ice sublimates. The resulting equilibrium sublimation mass flux is $F_s = 4{\times}10^{-5}$ kg m^{-2} s^{-1}, which represents a maximum in the sense that the subsolar temperature is the highest possible temperature on the body.

The area of sublimating surface needed to supply mass loss at rate dM_d/dt [kg s^{-1}] is given by

$$\pi r_s^2 = \left(\frac{1}{f_{dg} F_s}\right) \frac{dM_d}{dt} \tag{15}$$

where r_s is the radius of a circle having area equal to the sublimating area and f_{dg} is the ratio of dust to gas production rates. In earlier work (Hsieh et al. 2004) we assumed f_{dg} =1, as was traditional in cometary studies before long wavelength observations made possible the accurate measurement of dust masses in comets. However, recent measurements of short-period comets have convincingly shown $f_{dg} > 1$. For example, infrared observations of comet 2P/Encke, whose orbit is closest to that of 133P among the short-period comets, give $10 \leq f_{dg} \leq 30$ (Reach et al. 2000). Values $f_{dg} > 1$ are physically possible because the ejected dust, although carrying more mass than the driving gas, travels much more slowly, allowing momentum to be conserved. We conservatively take $f_{dg} = 10$ and, with $0.2 \leq dM_d/dt \leq 1.4$ kg s^{-1} use Equation (15) to obtain $500 \leq \pi r_s^2 \leq 3500$ m^2, corresponding to a circular, sublimating patch on the surface with radius $13 \leq r_s \leq 33$ m. Evidently, only a very tiny fraction of the nucleus surface ($r_s^2/r_n^2 \sim$ (1 to 5)$\times 10^{-5}$) of exposed ice is needed to supply the dust mass loss in 133P.

The tiny size of the active area affects the dust speed, as we now show. Outflow of the gas into the surrounding half-space vacuum will produce a wind that exerts a drag force on entrained dust particles. If outgassing occurred from a point source, the gas density would fall in proportion to d^{-2}, where d is the distance from the source. If outgassing occurred from an infinite plane, the gas density would vary as d^0, for the same reason that the surface brightness of an extended light source is independent of the distance from which it is viewed. The intermediate case, in which the source is neither a point nor an infinite plane, requires a full gas dynamic treatment to determine the iso-density surfaces in the expanding gas, which lies beyond the aims of the present work.

Instead, we have made a "small source approximation" (SSA) model as described in the Appendix. Its solution is plotted in Figure (12), where it is compared with the Whipple

model. For both the SSA and the Whipple models, we plot two curves. The upper curves (solid lines) show the terminal dust speeds in the absence of nucleus gravity while the lower curves (dashed lines) show the full solutions including gravity. The SSA velocity law has a form similar to Whipple's formula for the speed of an escaping particle, but differs in that the source size, r_s, now plays a role in the terminal velocity, with smaller r_s corresponding to lower ejection speeds. Physically, the difference between our result and Whipple's is the length scale over which gas drag accelerates entrained dust particles. Whipple assumed that sublimation was uniform from the entire sun-facing hemisphere and so, in his model, the length scale is the radius of the nucleus, r_n. In our model, the length scale is the (much smaller) size of the source, r_s. In simple terms, the difference between the models is the difference between a handgun and a rifle; the latter fires a faster bullet than the former because the longer barrel gives a greater acceleration length over which momentum from the explosive gases is transferred to the projectile.

While the SSA model gives lower speeds than the Whipple model, the predicted grain speeds are still about an order of magnitude larger than those measured in 133P (Figure 12). We see several possibilities for explaining this difference. One possibility is that F_s is over-estimated because the ice is not located exactly at the subsolar point. Ice might also be protected beneath a thin refractory mantle where it would receive only a fraction of the full solar insolation, reducing F_s. Of course, a severe reduction in the sublimation flux would further reduce the critical grain size, a_c, magnifying the puzzle of how millimeter and centimeter sized grains can be ejected.

Another possibility is that sublimation proceeds, not from a single patch of radius r_s, but from a large number of sources individually small compared to r_s, but having a combined area πr_s^2, such that V_T from Equation (20) is further reduced. This might be a natural result of progressive mantle growth on an aging ice surface, as larger blocks left behind on the surface restrict sublimation to a network of small, unblocked areas. By Equation (20), an order of magnitude reduction in dust speed to match the measured values would be produced by sublimation from individual sources of scale $r_s \sim 0.2$ m.

Yet another possibility is that ejected dust particles leave the surface containing some fraction of attached ice, the anisotropic sublimation of which would exert a reaction ("rocket") force, propelling the grains laterally out of the gas flow. Small, spherical dust grains should be essentially isothermal, giving no net force, but an irregular distribution of ice within a porous, aspherical, rotating grain will in general lead to a net sublimation force even from an isothermal particle. A very modest ice fraction in each grain would be sufficient to propel the particles laterally over distances $\gtrsim r_s$, especially in 133P where $r_s \sim 20$ m is so small. The process would be less important on more active (generally better studied) comets because of

their larger source regions. Unfortunately, the data offer no way to determine whether these effects, working either separately or collectively, occur in 133P.

It is highly improbable that gas drag acting alone could launch particles from the nucleus into the dust tail with terminal velocities (i.e. velocities at distances $r \gg r_n$) much smaller than the gravitational escape speed from the nucleus. In order to climb out of the gravitational potential well of the nucleus while retaining a terminal velocity $V_T(a)$, dust grains must be launched from the surface at speed $V = (V_T(a)^2 + V_e^2)^{1/2}$, where $V_e \sim 1.8$ m s^{-1} is the gravitational escape speed from 133P. For example, millimeter grains by Equation (6) have $V_T(a) \sim 6$ cm s^{-1}, from which the above relation gives a launch velocity $V \sim 1.801$ m s^{-1} (i.e. only 0.05% larger than V_e). Gas drag alone is unable to provide such fine-tuning of the ejection velocity over a wide range of particle sizes.

The solution to this problem may be that gravity is nearly or completely negated by centripetal acceleration on parts of 133P, as a result of the elongated shape and 3.5 hr rotation period. We envision very weak gas flow driven by sublimation near the tips of the elongated nucleus, perhaps in the form of a fluidized bed on which gravity is reduced nearly to zero. In this scenario, the particles would accelerate by gas drag according to a $V \propto a^{-1/2}$ velocity-size relation, consistent with the data. Their escape would be unimpeded by gravity so that even the largest, slowest particles could escape to be swept up by radiation pressure. Forces other than gas drag might eject particles under these circumstances, but only sublimation can account for the observed seasonal modulation of the activity on 133P, as originally proposed (Hsieh et al. 2004). In this regard, 133P is a C-type object (Hsieh et al. 2004) and, as noted above, must have density $\rho_n \gtrsim 1300$ kg m^{-3} (Equation 2) if regolith material is to be gravitationally bound at its rotational extremities. We note that the average density of C-type asteroids is 1300±600 kg m^{-3} (Cary 2012), consistent with ρ_n. A hybrid solution in which gas drag provides the force to expel particles with rotation reducing the potential barrier is thus plausible, although not proved.

6. SUMMARY

We present new, time-resolved observations of main-belt comet 133P/Elst-Pizarro when in an active state on 2013 July 10. The new data allow us to examine 133P at unprecedented resolution (Nyquist-sampled resolution is 0.08″ corresponding to 120 km at 133P).

1. The principal manifestation of activity in 133P is an anti-sunward tail $>9\times10^4$ km in length and <800 km in width. The tail consists of dust particles released at low-speeds from the nucleus no earlier than five months prior to the Hubble observation and swept away from it by solar radiation pressure. A previously unobserved, ultralow surface brightness sunward tail, $\sim10^3$ km in linear extent, consists of centimeter-sized and larger particles released in a previous orbit. There is no resolved coma.

2. The best-fit models involve continuous emission, for periods of months, of dust at rates 0.2 to 1.4 kg s^{-1}. These rates are so small that they could be sustained by the nucleus for billion-year timescales provided the duty-cycle is $\lesssim 10^{-3}$.

3. The main parameters of the nucleus determined from HST data (absolute magnitude $H_V = 15.70\pm0.10$, equivalent circular radius $r_n = 2.2\pm0.4$ km, axis ratio ∼1.5:1, semi-axes 2.7 × 1.8 km and rotation period ∼3.5 hr) are compatible with earlier determinations from ground-based data.

4. Characteristic dust speeds are $V \sim 1.8\ a_{\mu m}^{-1/2}$ m s^{-1}, where $a_{\mu m}$ is the particle radius in microns. Such low speeds are, in part, a consequence of the small source size and resulting limited coupling length on 133P, but additional effects must operate to reduce the dust speeds to the observed level.

5. The key properties of 133P are the seasonal emission of dust on timescales of months, the low speeds of ejected particles, their conformance to a $V \propto a_{\mu m}^{-1/2}$ velocity law and the absence of detected gaseous emission bands. We suggest a hybrid hypothesis in which dust is accelerated by weak gas flow due to sublimated water ice while dust ejection at sub-escape speeds is assisted by centripetal acceleration from rapid nucleus rotation. Acting separately, neither gas drag nor centripetal effects can account for the key properties of 133P. While the hybrid hypothesis remains conjectural, no plausible alternative has been identified.

We thank Henry Hsieh, Pedro Lacerda and the anonymous referee for comments on this manuscript. We thank Alison Vick, Tamas Dahlem and other members of the STScI ground

system team for their expert help in planning and scheduling these Target of Opportunity observations. Based on observations made with the NASA/ESA *Hubble Space Telescope,* with data obtained at the Space Telescope Science Institute (STScI). Support for program 13005 was provided by NASA through a grant from the Space Telescope Science Institute, which is operated by the Association of Universities for Research in Astronomy, Inc., under contract NAS 5-26555. Other support was provided by NASA's Planetary Astronomy program.

7. Appendix: The Small Source Approximation

The "small source approximation" is a toy model intended to capture the physical essence of a complicated gas dynamics problem. The geometry is shown Figure 13, with a dust particle located at point P along a line connecting the nucleus center with the center of the dust source. Off-axis motions are not considered and we assume that dust speed $V \ll V_g$, the gas speed. We represent the source by a surface patch of horizontal radius r_s (c.f. Equation 15) and represent the gas density at distance, d, above the source by

$$\rho_g(d) = \rho_g(r_n) \left[\frac{r_s}{d + r_s} \right]^2 \tag{16}$$

where $\rho_g(r_n)$ is the gas density at the sublimating surface. This function has the desirable properties that $\rho_g(d) \propto d^{-2}$ for $d \gg r_s$, while, $\rho_g(d) \propto d^0$ for $d \ll r_s$, .

The dust particle is separated from the center of the nucleus by distance r. The nucleus has radius r_n and therefore $d = r - r_n$. A dust particle of radius a intercepts momentum from gas sweeping past at speed V_g at the rate $C_D \rho_g(d) \pi a^2 V_g^2/2$, where $C_D \sim 1$ is a dimensionless drag coefficient that depends on the shape and nature (e.g. compact vs. fluffy) of the grain. The mass of the dust grain is just $4/3\pi\rho a^3$, where ρ is the grain density. The acceleration of the grain due to gas drag is therefore

$$\alpha = \frac{3 C_D V_g^2 \rho_g(r_n)}{8 \rho a} \left[\frac{r_s}{r + r_s - r_n} \right]^2 \tag{17}$$

In addition, the grain experiences a downward acceleration due to gravity, $-GM_n/r^{-2}$, where M_n is the mass of the nucleus. The equation of motion can then be written

$$V \frac{dV}{dr} = \frac{3 C_D V_g^2 \rho_g(r_n)}{8 \rho a} \left[\frac{r_s}{r + r_s - r_n} \right]^2 - \frac{G M_n}{r^2} \tag{18}$$

Integrating from the surface of the nucleus, $r = r_n$ where $V = 0$, to $r = \infty$, where $V = V_T$,

$$\int_0^{V_T} V dV = \int_{r_n}^{\infty} \left(\frac{3 C_D V_g^2 \rho_g(r_n)}{8 \rho a} \left[\frac{r_s}{r + r_s - r_n} \right]^2 - \frac{G M_n}{r^2} \right) dr \tag{19}$$

Noting that $\rho_g(r_n) = F_s(r_n)/V_g$, and writing $M_n = 4/3\pi\rho_n r_n^3$, where ρ_n is the density of the nucleus, we obtain an expression for the terminal velocity in the SSA:

$$V_T = \left(\frac{3 C_D V_g F_s(r_n) r_s}{4 \rho a} - \frac{8 \pi G \rho_n r_n^2}{3} \right)^{1/2} \tag{20}$$

which is plotted in Figure (12). Setting the left hand side of Equation (20) equal to zero gives the critical size

$$a_c = \frac{9 C_D V_g F_s(r_n) r_s}{32 \pi G \rho_n \rho r_n^2} \tag{21}$$

above which dust particles are too heavy to be ejected by gas drag. Substituting values appropriate for 133P, we find $a_c \sim 0.1$ mm. Again, C_D and the densities ρ and ρ_n are unmeasured and could easily each be wrong by a factor of 2 or more.

REFERENCES

Agarwal, J., Müller, M., & Grün, E. 2007, Space Sci. Rev., 128, 79

Bagnulo, S., Tozzi, G. P., Boehnhardt, H., Vincent, J.-B., & Muinonen, K. 2010, A&A, 514, A99

Burns, J. A., Lamy, P. L., & Soter, S. 1979, Icarus, 40, 1

Carry, B. 2012, Planet. Space Sci., 73, 98

Chesley, S. R., Kaluna, H., Kleyna, J., et al. 2010, Bulletin of the American Astronomical Society, 42, 950

Drilling, J. S., & Landolt, A. U. 2000, in Allen's Astrophysical Quantities, ed. A. N. Cox (New York: Springer) 381

Gilbert, A. M., & Wiegert, P. A. 2010, Icarus, 210, 998

Harmon, J. K., Nolan, M. C., Ostro, S. J., & Campbell, D. B. 2004, Comets II, University of Arizona Press, Tucson, p. 265

Harris, A. W. 1996, Lunar and Planetary Institute Science Conference Abstracts, 27, 493

Hsieh, H. H. 2009, A&A, 505, 1297

Hsieh, H. H., Jewitt, D. C., & Fernández, Y. R. 2004, AJ, 127, 2997

Hsieh, H. H., & Jewitt, D. 2006, Science, 312, 561

Hsieh, H. H., Jewitt, D., & Fernández, Y. R. 2009, ApJ, 694, L111

Hsieh, H. H., Jewitt, D., & Ishiguro, M. 2009, AJ, 137, 157

Hsieh, H. H., Jewitt, D., Lacerda, P., Lowry, S. C., & Snodgrass, C. 2010, MNRAS, 403, 363

Hsieh, H. H., Meech, K. J., & Pittichová, J. 2011, ApJ, 736, L18

Hsieh, H. H., Pohlen, M., & Matulonis, A. 2013, Central Bureau Electronic Telegrams, 3564, 1

Ishiguro, M., Sarugaku, Y., Ueno, M., et al. 2007, Icarus, 189, 169

Ishiguro, M., et al. 2013, in press

Jewitt, D. 2012, AJ, 143, 66

Jewitt, D. C., & Meech, K. J. 1987, ApJ, 317, 992

Kimura Hiroshi, & Liu Cai-pin 1977, Chinese Astronomy, 1, 235

Krist, J. E., Hook, R. N., & Stoehr, F. 2011, Proc. SPIE, 8127,

Levison, H. F., Bottke, W. F., Gounelle, M., et al. 2009, Nature, 460, 364

Mottl, M., Glazer, B., Kaiser, R., & Meech, K. 2007, Chemie der Erde / Geochemistry, 67, 253

Nesvorný, D., Bottke, W. F., Vokrouhlický, D., et al. 2008, ApJ, 679, L143

Reach, W. T., Sykes, M. V., Lien, D., & Davies, J. K. 2000, Icarus, 148, 80

Sonnett, S., Kleyna, J., Jedicke, R., & Masiero, J. 2011, Icarus, 215, 534

Toth, I. 2006, A&A, 446, 333

Waszczak, A., Ofek, E. O., Aharonson, O., et al. 2013, MNRAS, 433, 3115

Weaver, H. A., Feldman, P. D., Merline, W. J., et al. 2010, A&A, 518, A4

Whipple, F. L. 1951, ApJ, 113, 464

This preprint was prepared with the AAS LaTeX macros v5.2.

Table 1. Observing Geometry

UT Date and Time	R[a]	Δ[b]	α[c]	θ_{-v}[d]	$\theta_{\odot}$[e]	$\delta_{\oplus}$[f]
2013 July 10d 06h 49m	2.725	2.060	18.7	248.7	246.8	-0.54

[a]Heliocentric distance, in AU

[b]Geocentric distance, in AU

[c]Phase angle, in degrees

[d]Position angle of the projected negative heliocentric velocity vector, in degrees

[e]Position angle of the projected anti-Solar direction, in degrees

[f]Angle of Earth above the orbital plane, in degrees

Table 2. Photometry

Image	UT[a]	t_i[b]	$V_{0.2}$[c]	$V_{1.0}$[d]	Δm[e]
1	16h 52m 38s	348	20.362	20.319	0.043
2	17h 00m 34s	348	20.348	–	–
3	17h 08m 30s	348	20.372	20.271	0.101
4	17h 17m 02s	348	20.538	20.483	0.055
5	17h 24m 58s	348	20.669	20.602	0.067
6	17h 32m 54s	252	20.766	20.701	0.065
7	18h 28m 18s	348	20.368	20.316	0.052
8	18h 36m 14s	348	20.354	20.306	0.048
9	18h 44m 10s	348	20.387	20.337	0.050
10	18h 52m 42s	348	20.441	20.390	0.051
11	19h 00m 38s	348	20.521	20.465	0.056
12	19h 08m 34s	252	20.611	20.542	0.069

[a]UT start time of the integration on 2013 July 10

[b]Integration time, seconds

[c]Apparent V magnitude within 5 pixel ($0.2''$) radius aperture

[d]Apparent V magnitude within 25 pixel ($1.0''$) radius aperture

[e]$\Delta m = V_{0.2} - V_{1.0}$

Table 3: Dust Model Parameters[a]

Parameter	Parameter Range Explored	Best-fit values	Unit
q	3 to 4 with 0.25 interval	CM: 3.25 to 3.50	
		IM: 3.15±0.05	
t_0	10 to 200 with 10 interval	CM: 36 to 150	days
		IM: 36 to 70	days
t_1	CM: t_1=0	fixed	days
	IM: t_1=t_0-1	fixed	days
$\beta_{\rm max}$[b]	1×10^{-3} to 1[d]	CM: $\geq7\times10^{-2}(t_0=36)$ to $3\times10^{-3}(t_0=150)$	–
		IM: $\geq3\times10^{-3}(t_0=36)$ to $1\times10^{-3}(t_0=70)$	–
$\beta_{\rm min}$[c]	5×10^{-6} to 5×10^{-2} [e]	CM: $\leq2\times10^{-3}(t_0=36)$ to $6\times10^{-5}(t_0=150)$	–
		IM: $\leq4\times10^{-4}(t_0=36)$ to $1\times10^{-4}(t_0=70)$	–
V_1	1.5 $\sin^{-1} w$	fixed	m s^{-1}
u_1	1/2	fixed	
k	-3	fixed	–
σ_v	0.3	fixed	–
w	90	fixed	degree

[a] CM: Continuous ejection model, IM, Impulsive ejection model

[b] The smallest value of β_{max} needed to fit the data

[c] The largest value of β_{min} needed to fit the data

[d] 1/40 of full range in logarithmic space

[e] 1/30 of full range in logarithmic space

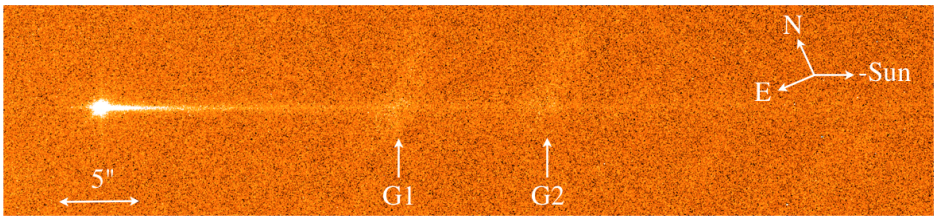

Fig. 1.— Composite F350LP image of 133P having total integration time 3984 seconds. A long, thin dust tail extends from the nucleus, visible at left. G1 and G2 mark field galaxies imperfectly removed from the data. The antisolar direction is marked. This is indistinguishable from the direction of the projected negative velocity vector at the resolution of the Figure (see Table 1).

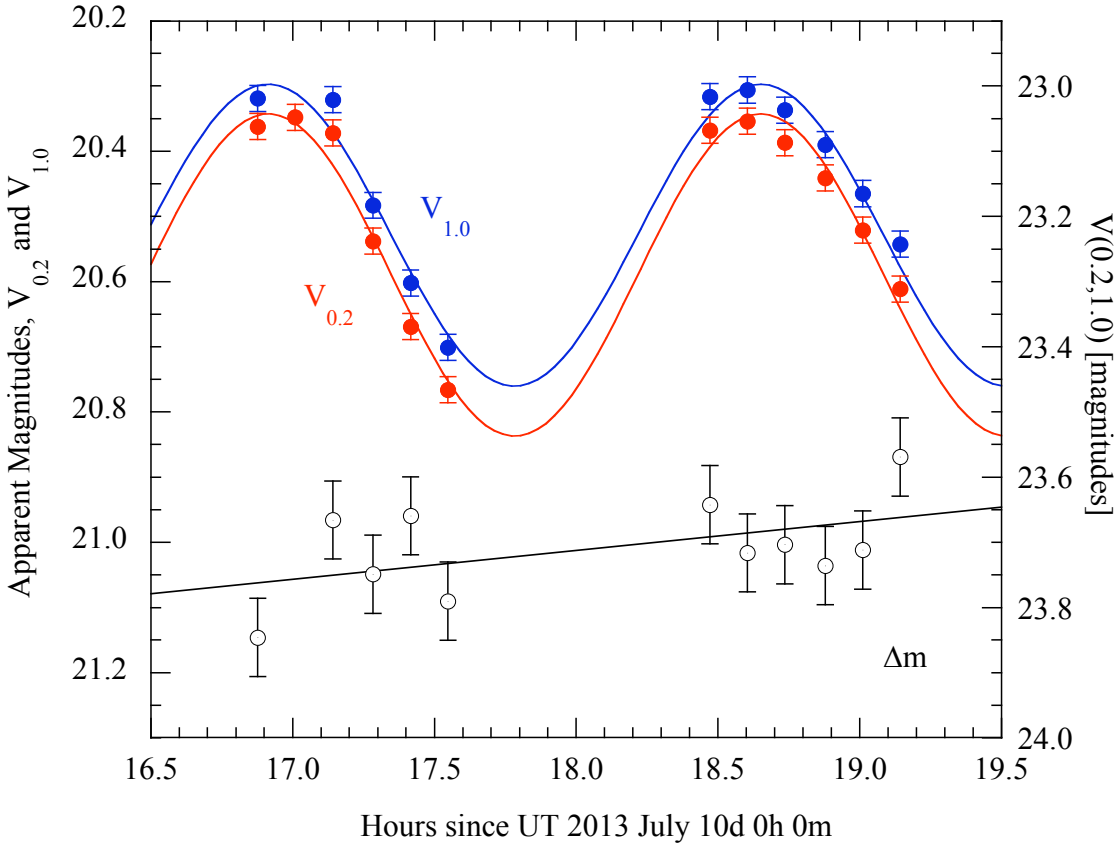

Fig. 2.— Rotational lightcurve of 133P showing $V_{0.2}$ as red circles and $V_{1.0}$ as blue circles. Red and blue lines mark the best-fit sinusoids and are added to guide the eye. The magnitude of the material between the two apertures is also shown (black empty circles and right-hand vertical axis). The black straight line is a least-squares fit to the data.

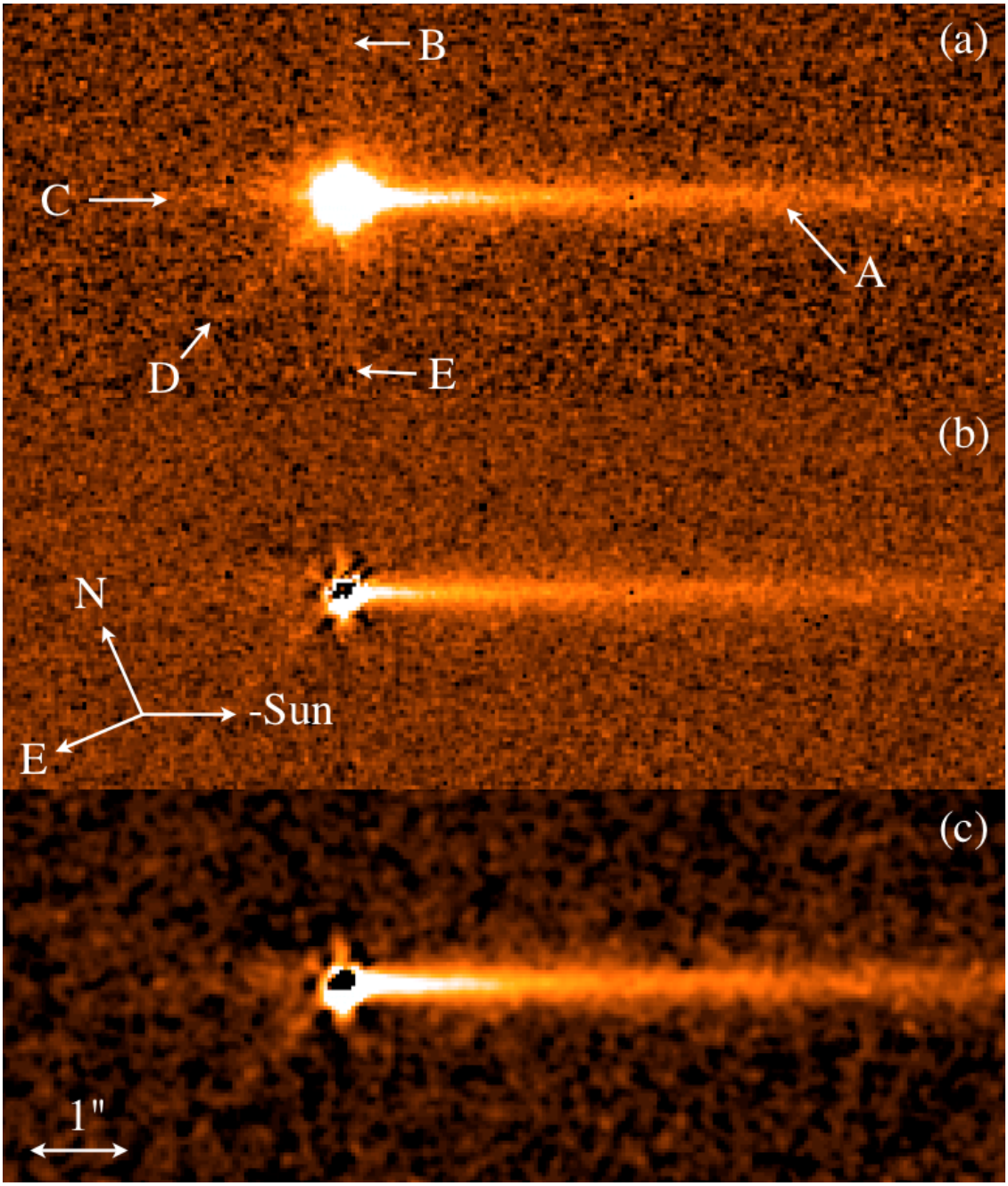

Fig. 3.— (a) Near-nucleus region of the composite F350LP image from Figure 1. Of the features labeled A-E, B and E are diffraction spikes, D is a charge-transfer efficiency artifact in the CCD and only A and C are true dust features associated with 133P. (b) Same image but with a centered, scaled model of the Hubble PSF subtracted (c) Gaussian-convolved and heavily-stretched version of (b) to show residual emission at locations of C and D. A 1″ scale bar is shown.

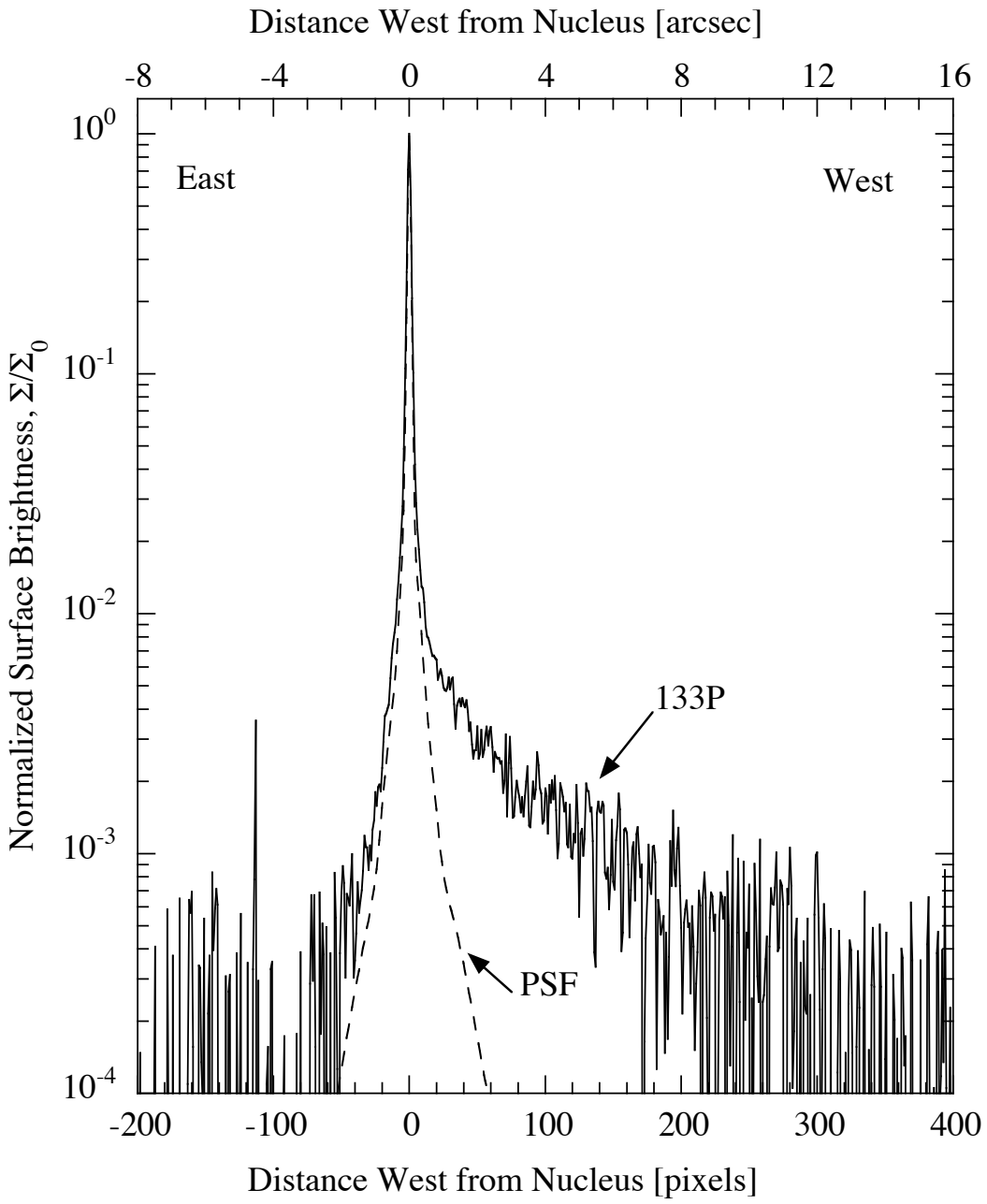

Fig. 4.— Surface brightness of 133P (solid line) and the PSF (dashed line) shown as a function of distance from the nucleus. The surface brightnesses are the average within a 41 pixel (1.64″) wide strip centered on the tail. The peak surface brightness corresponds to Σ_0 = 15.80 mag. (arcsec)$^{-2}$. Negative coordinates are east of the nucleus.

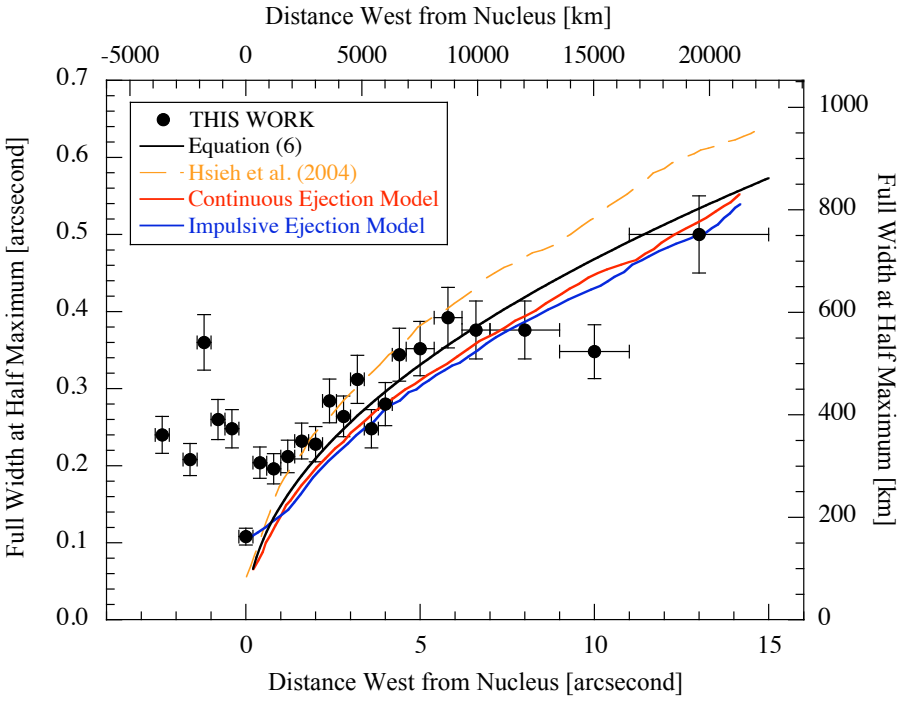

Fig. 5.— Full width at half maximum of the dust tail as a function of distance measured west from the nucleus. Vertical error bars show the estimated ±10% uncertainties in FWHM. Horizontal bars mark the range of distances over which each FWHM was measured, increasing as the tail grows fainter. The black circles show measurements from the 2013 July 10 HST data. The model of Hsieh et al. (2004) is marked as an orange, dashed line. The red curve shows continuous emission from the date of observation to $t_0 = 150$ days before, with $q = 3.25$ and $\beta_{min} = 5{\times}10^{-5}$. The blue curve shows impulsive emission occurring 70 days before the HST observation, with $q = 3.15$ and $\beta_{min} = 10^{-4}$.

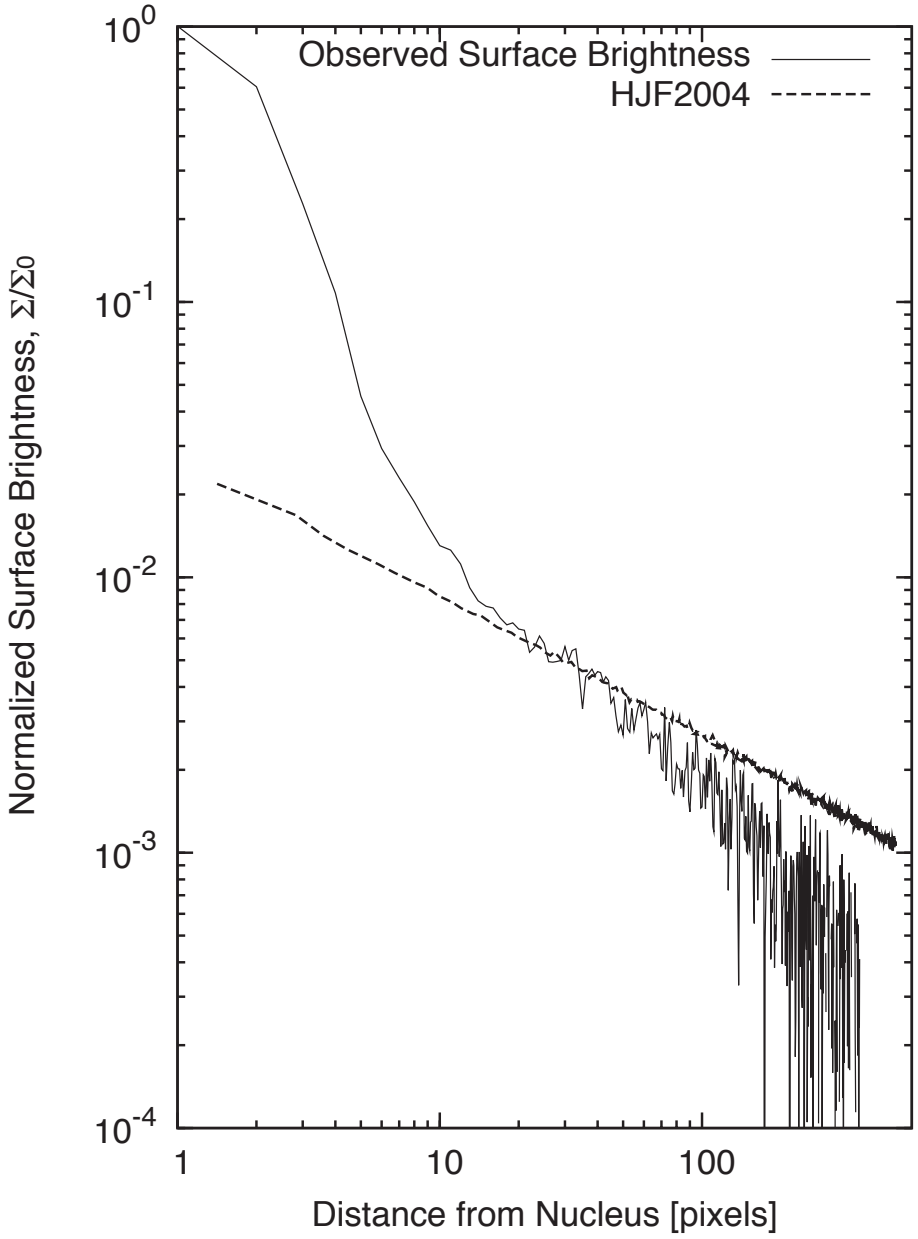

Fig. 6.— Surface brightness of 133P (solid line) shown as a function of distance from the nucleus. A model computed using dust parameters derived in Hsieh et al. (2004) is shown as a dashed line.

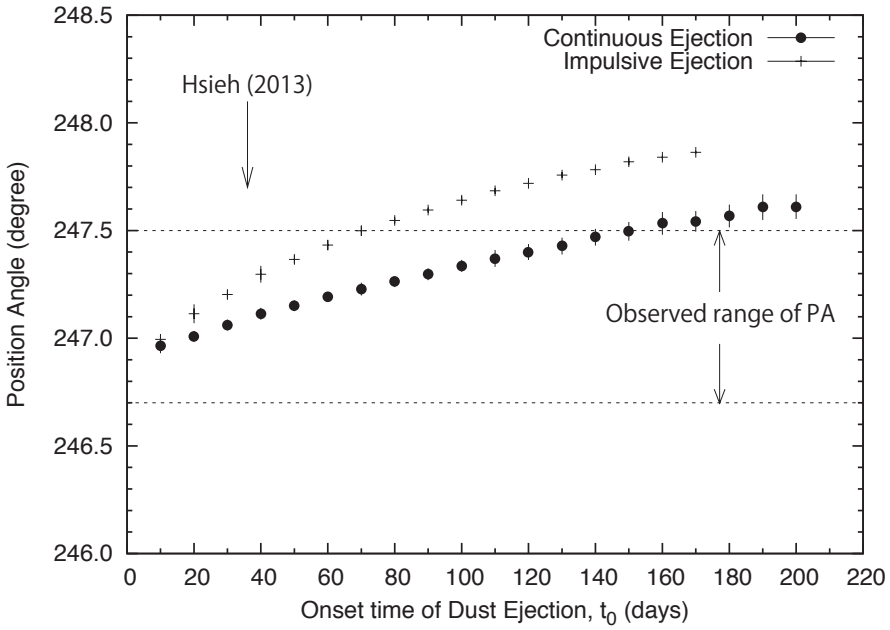

Fig. 7.— Tail position angles as a function of the onset time of dust ejection, t_0 (see Equation 10). The observed range of position angle is shown by dashed lines, and the time of the first detection of 133P tail in 2013 appearance (Hsieh et al. 2013) is shown by a vertical arrow.

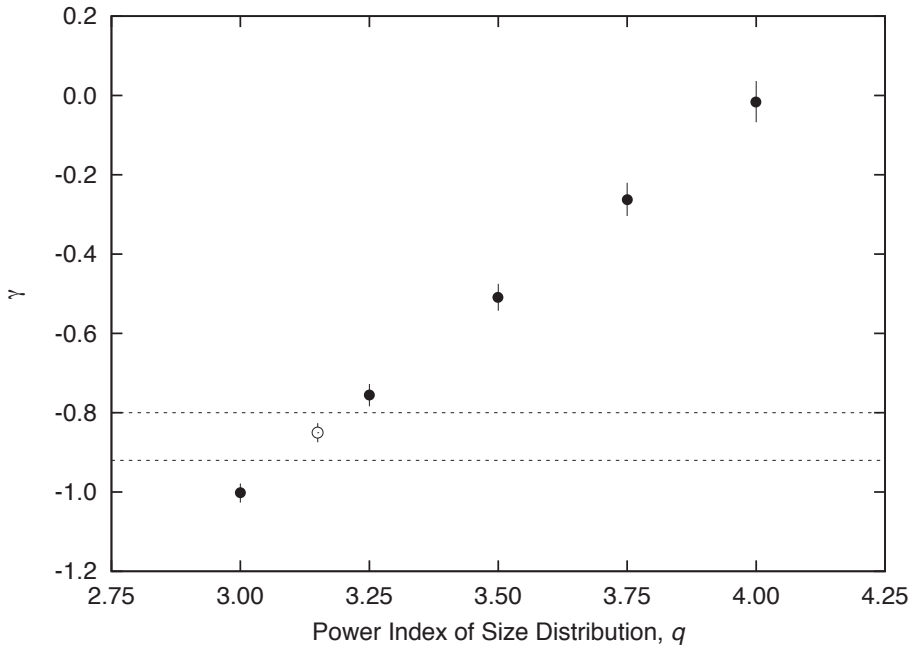

Fig. 8.— Power index of the surface tail brightness distribution γ vs power index of particle size distribution q. Filled circles are derived from our model simulations with parameters in Table (3). The dashed lines show the upper and lower limits from our observation. Open circle was obtained by the additional simulation with q=3.15. The errors correspond to 3σ of the simulation results.

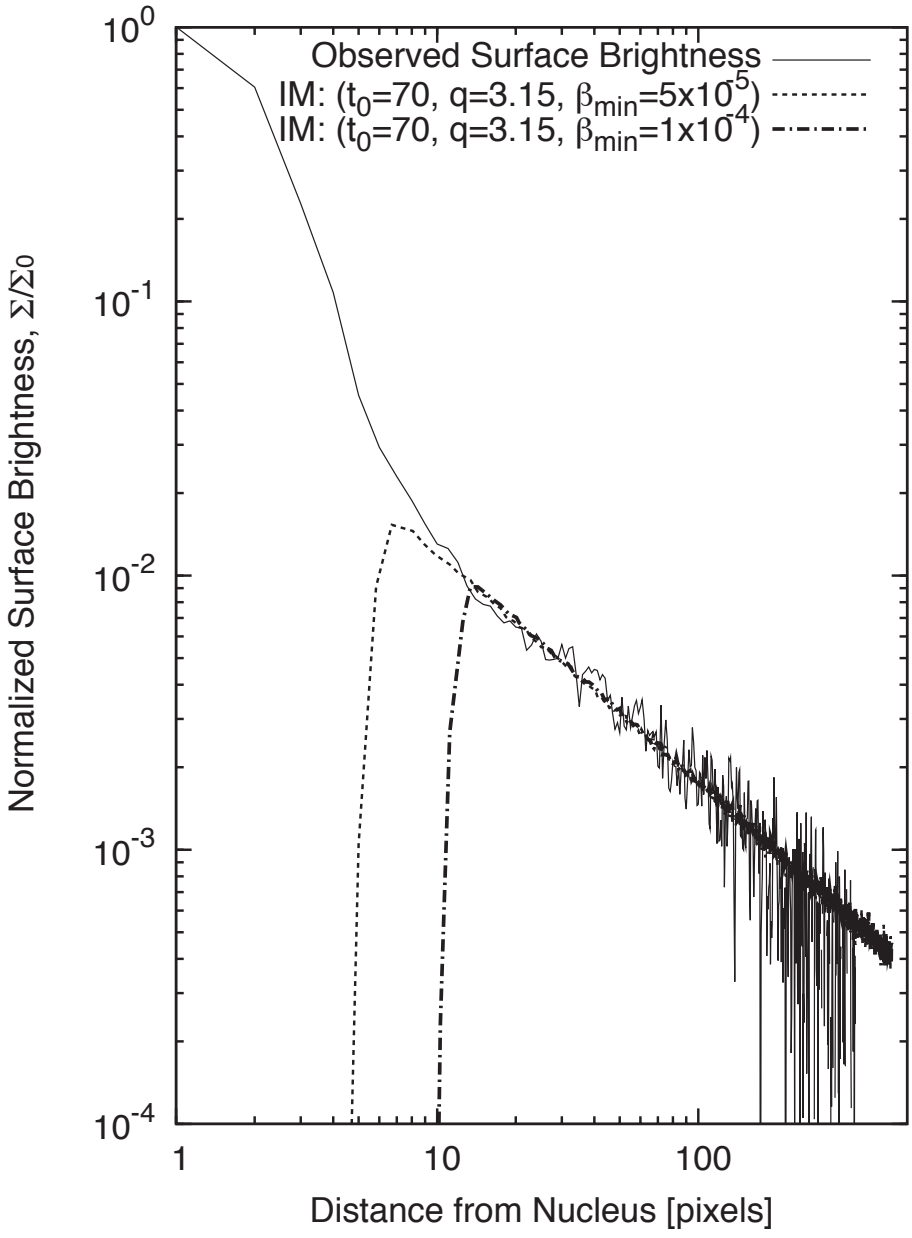

Fig. 9.— Surface brightness of 133P (solid line) and impulsive models showing the effect of maximum particle size.

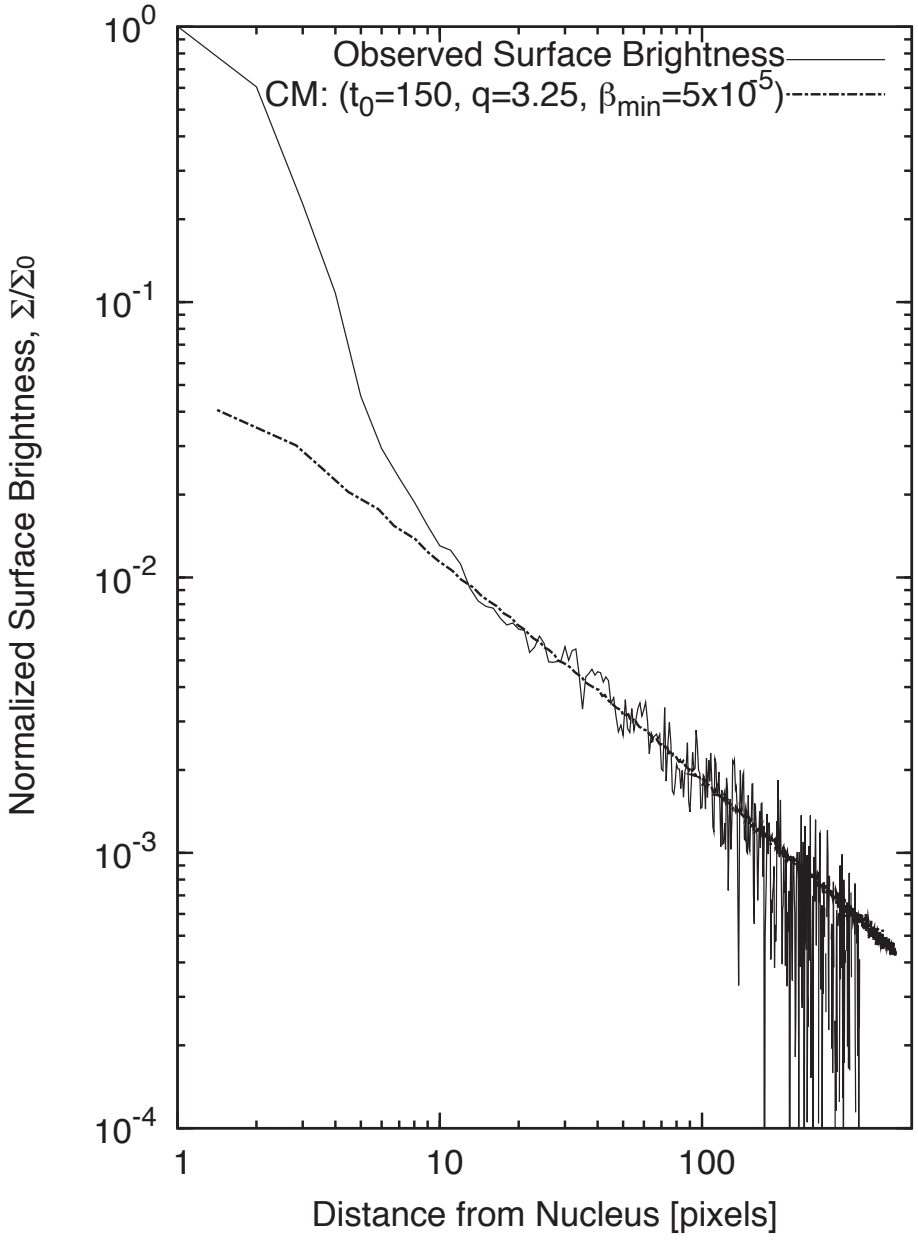

Fig. 10.— Surface brightness of 133P (solid line) and a model in which dust is ejected continuously starting 150 days before the HST observation on July 10.

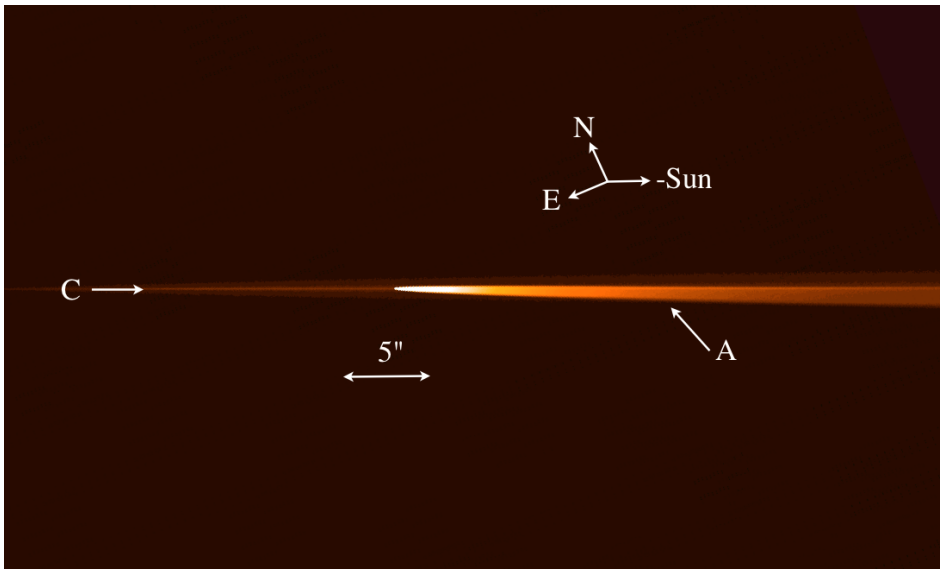

Fig. 11.— Model of neckline structure (C) (c.f. Figure 3). The neckline structure best seen to the East of the nucleus consists of particles ejected 5.5 years (i.e. one orbit period) before the epoch of the HST observations, with $\beta_{min} = 10^{-5}$. The main tail "A" is also marked.

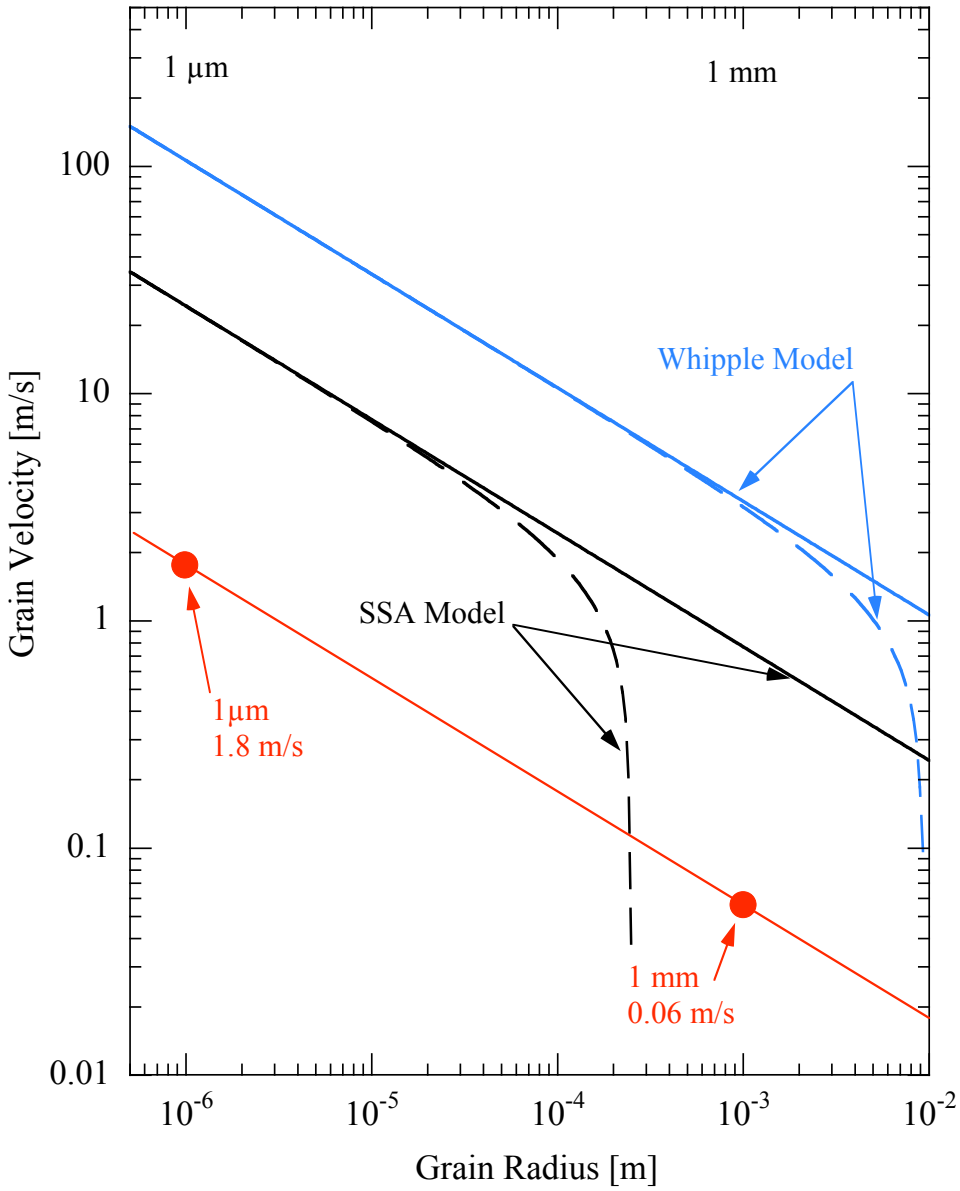

Fig. 12.— Models of the dust grain ejection velocity from 133P as a function of particle radius. For both SSA (Appendix) and Whipple models, we plot two curves. The upper (solid) lines show the terminal velocity that would be achieved in the absence of nucleus gravity. The lower (dashed) lines show the full solutions including gravity. The red line shows Equation (6) while the red circles mark speeds of 1 μm and 1 mm dust particles measured in 133P.

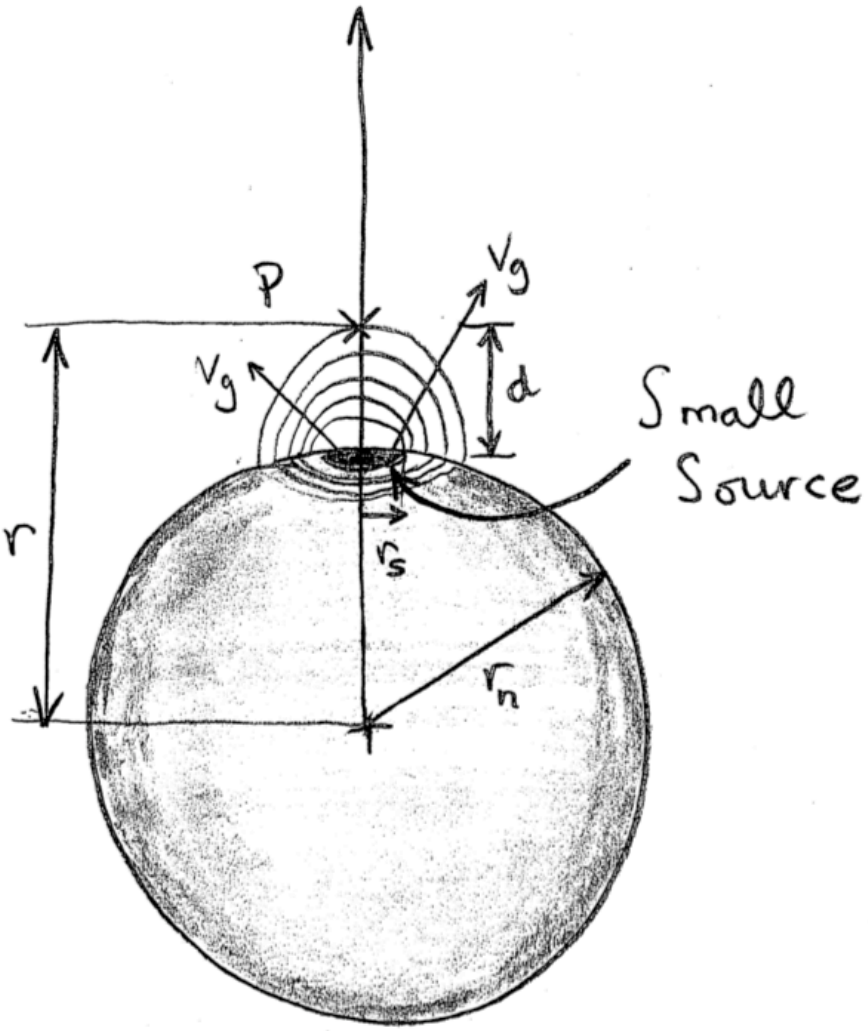

Fig. 13.— Schematic diagram showing the geometry assumed in the Small Source Approximation. Dust particle P is located at distance r from the center of a spherical nucleus of radius r_n, at height $d = r - r_n$ above the surface. Sublimated gas streams outward at speed V_g from a surface patch of radius $r_s \ll r_n$. See Appendix for a detailed discussion.